Nanoindentation of tungsten: From interatomic potentials to dislocation plasticity mechanisms

F. J. Domínguez-Gutiérrez,[1] P. Grigorev,[2] A. Naghdi,[1] J. Byggmästar,[3] G. Y. Wei,[3,4] T. D. Swinburne,[2] S. Papanikolaou,[1] and M. J. Alava[1,5]

[1]*NOMATEN Centre of Excellence, National Center for Nuclear Research, 05-400 Swierk/Otwock, Poland*
[2]*Aix-Marseille Universite, CNRS, CINaM UMR 7325, Campus de Luminy, 13288 Marseille, France*
[3]*Department of Physics, University of Helsinki, P.O. Box 43, FI-00014, Finland*
[4]*Henan Academy of Big Data, Zhengzhou University, Zhengzhou 450052, China*
[5]*Department of Applied Physics, Aalto University, P.O. Box 11000, 00076 Aalto, Espoo, Finland*

(Received 25 January 2023; accepted 17 March 2023; published 24 April 2023)

In this study, we employed molecular dynamics simulations, both traditional and machine learned, to emulate spherical nanoindentation experiments of crystalline W matrices at different temperatures and loading rates using different approaches, such as EAM, EAM with Ziegler, Biersack, and Littmark corrections, modified EAM, analytic bond-order approach, and a recently developed machine-learned tabulated Gaussian approximation potential (tabGAP) framework for describing the W-W interaction and plastic deformation mechanisms. Results showed similarities between the recorded load-displacement curves and dislocation densities, for different interatomic potentials and crystal orientations at low and room temperature. However, we observe concrete differences in the early stages of elastic-to-plastic deformation transition, revealing different mechanisms for dislocation nucleation and dynamics during loading, especially at higher temperatures. This is attributed to the particular features of orientation dependence in crystal plasticity mechanisms and, characteristically, the stacking fault and dislocation glide energies information in the interatomic potentials, with tabGAP being the one with the most well-trained results compared to density functional theory calculations and experimental data.

DOI: 10.1103/PhysRevMaterials.7.043603

I. INTRODUCTION

Nanoindentation is a technique used to measure the mechanical properties of a potential candidate material at the nanoscale for applications at extreme operating conditions. It entails using a small, sharp tip into the sample surface to measure the force required to do so and the resulting displacement into the material [1–4]. A pop-in event that defines the elastic to plastic deformation transition is produced as the indenter tip starts to penetrate the surface; it is often used as a reference point for analyzing the mechanical behavior of a material, as it can provide insight into the internal structure of the sample, which gives the opportunity to explore the mechanisms of plastic deformation initiation responsible for modification of mechanical properties of the material [5]. In addition, nanoindentation-induced plastic patterning is a process that involves the creation of patterns or structures in a material at the nanoscale with a wide range of applications, including the fabrication of nanostructured surfaces with enhanced functionalities and the development of new materials with tailored mechanical properties [6]. Plastic patterning due to nanoindentation is highly affected by the applied load, surface orientation, temperature, and the properties of the material itself, which needs a fundamental understanding of the materials deformation at the plastic zone beneath the indented surface region [2].

Tungsten is a refractory BCC material that can mechanically sustain extreme operating conditions due to its high melting point, low sputtering yield, and low tritium inventory [7–11]. W is often used in the production of high-strength steel alloys, as well as in the manufacturing of tungsten carbide, which is a very hard and durable material used in cutting tools and wear-resistant products, besides being the main candidate to design a plasma facing component (PFM) for the next generation of fusion reactors [12–15] experiencing a harsh environment due to the hydrogen/deuterium ions irradiation from the fusion plasma that causes indentation size effects at a scale of 100 nm. Moreover, ISO:14577 provides guidelines for the use of spherical indentation techniques and defines W to have a high elastic modulus which makes it a reference material for indirectly calibrating nanomechanical test instruments [16]. Therefore, it is necessary to study the relationship between indentation load-displacement curves and the evolution of the surface plastic patterning formation in order to better understand the plastic deformation mechanism of W matrices and its alloys. Atomistic simulations based on molecular dynamics (MD) can provide information about plastic deformation mechanisms, although there are limitations in some cases. These simulations are now capable of saving financial and technological resources [1–3,16–22].

The goal of our work is to explore the advantages and limitations of several EAM-based interatomic potentials reported in the literature for describing plastic deformation of tungsten at the early stages of the nanoindentation test, where experimental observation is currently inaccessible. Our objective is to investigate the role of the most used interatomic potentials in nanoindentation test modeling, where the mechanisms of dislocation nucleation and evolution are modeled differently. Despite similarities in the stress-strain curves and dislocation densities that are commonly utilized to characterize the

mechanical properties of a material, this work aims to provide an atomistic insight into the nanoindentation-induced plasticity of crystalline tungsten matrices using different approaches to model defect nucleation, as well as dislocation loop formation. Finally, we present an analysis of screw and junction dislocations using a nudged elastic band method (NEB) to clarify the differences in dislocation dynamics and surface plastic patterning in the MD simulation due to the chosen interatomic potential.

II. COMPUTATIONAL METHODS

In general, the EAM approach is used as a first attempt to computationally model the physical processes of the nanomechanical response of crystalline metals under external load. In this approach, the energy of the ith atom is defined as

$$E_i = \frac{1}{2}\sum_{j\in\mathcal{N}_i} V(r_{ij}) + F[\rho_i]. \tag{1}$$

Here $\mathcal{N}_i$ represents the atoms within the cutoff range, $V(r)$ is a pairwise potential, repulsive at short range, and $F[\cdot]$ is the embedding function for an atom in a region of electron density, given by $\rho_i = \sum_{j\neq i}\phi(r_{ij})$.

According to the OpenKIM project [23], there are more than 15 interatomic potentials for tungsten based on EAM. The one developed by Marinica *et al.* [24] (referred to as EAM2 by the authors in this work and labeled as **EAM**) has been reported to provide relatively good approximations to experimental values such as lattice constant measurements, cohesive energies of tungsten in the BCC phase, and elastic constants. This EAM potential has been evaluated by comparing it with DFT results for surface energy, dislocation core energy, and Peierls energy barrier calculations. The results show that, in general, this potential is a good choice for dislocation-involved simulations of tungsten, being commonly used to investigate dislocation nucleation in tungsten [25]. In addition, this potential has been used to develop potentials for tungsten with other metals, hydrogen, and carbides. For example, Wang *et al.* [26] used **EAM** potentials to develop W-H potentials.

The defect nucleation during nanoindentation load is important to model due to the inclusion of open boundaries in the MD simulations. Thus we consider an EAM potential developed by Mason *et al.* [27] that introduces smoothly varying, physically motivated modifications to the Ackland-Thetford potential [28] and adding $V_{\mathrm{ZBL}}(r)$ the Ziegler, Biersack, and Littmark (ZBL) universal screening potential contribution to improve vacancy- and surface-related properties. This potential, labeled as **EAM/ZBL**, was parametrized to improve the description of vacancy-type defects formation at different temperatures with vast surface properties aiming to model surface plastic patterning in a better way than EAM.

The correct description of the interaction of W-W and the intrinsic BCC crystal geometry of W is needed during the nanoindentation-induced dislocation nucleation. Thus we include in our work simulations with the modified-EAM that consider angular dependent interactions, which enter via the electron density term. These potentials were developed by Hiremath *et al.* [29] (labeled as **MEAM**) to investigate mechanisms of fracture in W samples providing an atomic insight, which also yields surface and unstable twinning energies that are in slightly better agreement with DFT than EAM results. This can help to describe the formation of twins during early stages of nanoindenation load simulations. Here, the total potential energy of the system is given as

$$E = \sum_i F_i(\overline{\rho}_i) + \sum_i \sum_{j\neq i} S_{ij}\phi_{ij}(r_{ij}), \tag{2}$$

where $F_i(\overline{\rho}_i)$ represents the embedding energy associated with placing the i atom into the background electron density $\overline{\rho}_i$. The function $\phi_{ij}(r_{ij})$ is defined as the pair interaction contribution between i and j atoms, separated by the distance r_{ij}, while S_{ij} is a screening function. The fitting process was done by using the open-source M-EAM parameter calibration (MPC) tool [30] to reproduce DFT data that serves as input data.

Another attempt to describe the W-W interaction in a material is the analytic bond-order potential (labeled as **ABOP** in this paper), which is a type of interatomic potential based on the concept of bond order measuring the strength of the chemical bond between atoms. It is constructed by fitting the potential energy of a system to a functional form that depends on the bond orders between atoms. In an analytic bond-order potential for W developed by Juslin *et al.* [31], the total energy is expressed as a sum over individual bond energies:

$$E = \sum_{i>j} V_{ij}^{\mathrm{R}}(r_{ij}) + b_{ij}V_{ij}^{\mathrm{A}}(r_{ij}), \tag{3}$$

where the pairlike repulsive, V^{R}, and attractive, V^{A}, terms are defined by Morse-type pair potentials and the bond-order parameter b_{ij} contains information of three-body contributions and angularity [32]. ABOP has several advantages over other EAM-based interatomic potentials capturing the effects of changes in bond order on the behavior of materials. Moreover, this bond-order potential includes second-neighbor interactions for pure tungsten samples and accurately captures the contributions of metallic W-W bonds. As discussed by the authors, the W potential provides a good description of the coordination dependence of structural parameters, cohesive energies, and surface properties, which are all important for nanoindentation modeling.

Nanoindentation simulations require detailed information of the material's surface due to open boundaries involved in the modeling. For this reason, we include the tabulated Gaussian approximation potential (**tabGAP**) in this work, which is a GAP machine-learning potential with enough surface information in the training data set being developed by Byggmästar *et al.* [33]. It has been trained with only simple low-dimensional descriptors (two-body, three-body, and an EAM-like density). The low dimensionality of the descriptors allows for creating faster tabulated versions, where the machine-learning energy contributions are mapped onto grids [34–36]. The total energy is then evaluated efficiently using

TABLE I. Value of elastic constants, shear modulus G, Poisson ratio ν, elastic modulus E (GPa), cohesive energy E_{coh} (eV/atom), and Burgers vector magnitude $|\vec{b}| = a_0\sqrt{3}/2$ (a_0 is the lattice constant) of tungsten. The last column is experimental values of C_{ij} [40] and G, ν, and E values [41].

Variable	EAM	EAM/ZBL	MEAM	ABOP	tabGAP	Expt.
C_{11}	523	511	527	541	524	501
C_{12}	203	201	194	191	200	198
C_{44}	160	161	177	162	148	151
G	160	161	177	162	135	130–160
ν	0.28	0.27	0.27	0.26	0.28	0.27–0.29
E	409	431	423	442	449	340–405
E_{coh}	−8.899	−8.9	−8.65	−8.89	−8.39	−8.9
$\|b\|$	2.72	2.75	2.74	2.74	2.75	2.74

cubic splines as

$$E_{\text{tot}} = \sum_{i<j}^{N} S_{ij}^{1\text{D}}(r_{ij}) + \sum_{i,j<k}^{N} S_{ijk}^{3\text{D}}(r_{ij}, r_{ik}, \cos\theta_{ijk}) + \sum_{i}^{N} S_{\text{emb}}^{1\text{D}}\left(\sum_{j}^{N} S_{\varphi}^{1\text{D}}(r_{ij})\right). \quad (4)$$

Here, $S_{ij}^{1\text{D}}(r_{ij})$ represents a one-dimensional cubic spline for the two-body contribution, $S_{ijk}^{3\text{D}}$ is the three-dimensional spline for the three-body contribution, and the final term is the embedding energy contribution similar to the EAM potentials. Despite the simplicity compared to other machine-learning potentials, the tabGAP achieves meV/atom accuracy for tungsten-based high-entropy alloys and compares well with DFT for various elastic, defect, and melting properties [33,36] that can be applied to model defect production at high temperatures [37].

To perform our simulations, we use the large-scale atomic/molecular massively parallel simulator (LAMMPS) software [38], which allows us to study the behavior of materials under a wide range of conditions. One of our goals is to accurately model plastic deformation, which is a crucial aspect of how materials respond to external loads. Thus we start by calculating the elastic constants C_{ij} and other properties of tungsten using different interatomic potentials that are presented in Table I noticing similar results in most respects and a good agreement with DFT calculations with $C_{11} = 520.35$ GPa, $C_{12} = 199.88$ GPa, and $C_{44} = 142.42$ GPa [39]. This information will help us understand how the interatomic potentials affect the mechanical behavior of the material and how they can be used to predict the response of tungsten to external loads. By studying these properties in detail, we hope to gain a deeper understanding of the underlying mechanisms of plasticity in tungsten.

Nanoindentation modeling

We first defined the initial W sample based on its crystal orientation, as shown in Table II. The FIRE (fast inertial relaxation engine) 2.0 protocol [42] is then used to optimize the energy of the sample and find the lowest energy structure.

TABLE II. Size of the numerical samples used to perform MD simulations. Sample size (d_x, d_y, d_z) in units of nm.

Orientation	[001]	[011]	[111]
d_x	37.92	34.76	33.52
d_y	41.08	37.99	33.52
d_z	31.60	36.65	46.52
Atoms	3 120 000	3 066 800	3 442 500
x axis	(100)	(100)	$(\bar{1}01)$
y axis	(010)	$(01\bar{1})$	$(1\bar{2}1)$
z axis	(001)	(011)	(111)

After that, we conducted an equilibration process for 100 ps using a Langevin thermostat at 77 and 300 K with a time constant of 100 fs [21]. This process continued until the system reached a homogeneous temperature and pressure profile with a density of 19.35 g/cm^3, which is in good agreement with the experimental value of 19.35 g/cm^3 [41]. In the first stage, the W samples are divided into three sections in the z direction to set up boundary conditions along its depth, d_z: (1) a frozen section with a width of approximately $0.02 \times d_z$, which was used for stability of the numerical cell, (2) a thermostatic section at approximately $0.08 \times d_z$ above the frozen section, which was used to dissipate the heat generated during nanoindentation, and (3) a dynamical atoms section, where the interaction with the indenter tip modifies the surface structure of the samples. In addition, a 5 nm vacuum section was included at the top of the sample as an open boundary [3].

The indenter tip is considered as a nonatomic repulsive imaginary (RI) rigid sphere with a force potential defined as $F(t) = K[\vec{r}(t) - R]^2$, where $K = 236$ eV/Å^3 (37.8 GPa) is the force constant and $\vec{r}(t)$ is the position of the center of the tip as a function of time, with radius $R = 6$ nm. We apply MD simulations using an NVE statistical thermodynamic ensemble and the velocity Verlet algorithm to emulate an experimental nanoindentation test. Periodic boundary conditions are set on the x and y axes to simulate an infinite surface, while the z orientation contains a fixed bottom boundary and a free top boundary in all MD simulations [21]. Here, $\vec{r}(t) = x_0\hat{x} + y_0\hat{y} + (z_0 \pm vt)\hat{z}$, with x_0 and y_0 as the center of the surface sample on the xy plane. The initial gap between the surface and the indenter tip, $z_0 = 0.5$ nm, moves with a speed of $v = 20$ m/s. The center of the indenter tip was randomly changed to 10 different positions to consider statistics in our results, resulting in a total of 150 MD simulations. Each process is performed for 125 ps with a time step of $\Delta t = 1$ fs. The maximum indentation depth is chosen to be 3.0 nm to avoid the influence of boundary layers in the dynamical atoms region. The load-displacement curve is then obtained by plotting the force on the indenter tip as a function of its displacement relative to the surface, as the indenter is driven into the material over time.

III. RESULTS

Figure 1 shows the recorded average load-displacement curves for nanoindentation loading of (001) W using the tabGAP framework at 77 and 300 K. Our results are in good

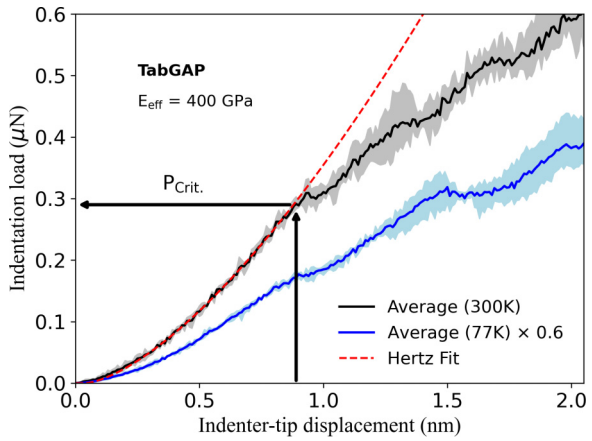

FIG. 1. Average nanoindentation load as a function of the displacement at 77 and 300 K as determined by the tabGAP framework. The color region represents the range of minimum and maximum load obtained from all MD simulations. Temperature has a significant impact on the plastic deformation mechanisms modeled by different approaches, as indicated by the Hertz fit curve that defines the critical load, P_{crit}. The results at 77 K are scaled by a factor of 0.6 for visualization.

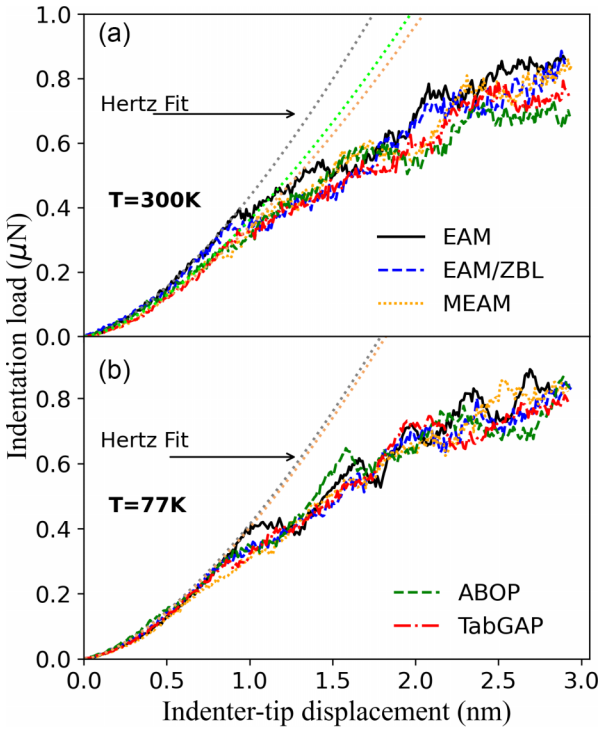

FIG. 2. Average load displacement curves from nanoindentation test by using different approaches at sample temperature of 300 in (a) and 77 K in (b). Hertz fitting curve is added to show the pop-in event. Temperature effects on surface morphology are shown by the elastic part where the surface information is required in the interatomic potentials.

qualitative agreement with the experimental data reported by Beake *et al.* [16,17]. These findings demonstrate the potential of the tabGAP framework in accurately reproducing results in the field of nanoindentation research. The average load is computed as $P_{\rm av} = 1/N \sum_i^N P_i$ with P_i as the load obtained from each MD simulation with random positions for the center of the indenter tip on the W surface. In our results, we include the maximum and minimum load as a function of indentation displacement from all MD simulations, represented by a colored region to show the statistical analysis in our work. The elastic nanocontact during loading process is characterized by a Hertz fitting curve based on the sphere-flat surface contact and expressed as

$$P_{\rm H} = \tfrac{4}{3} E_{\rm eff} R^{1/2} h^{3/2}, \tag{5}$$

where R is the indenter radius, h is the indenter displacement, and $E_{\rm eff}$ is the effective elastic modulus, where the tabGAP result of 400 GPa agrees well with experimental data [16]. The elastic to plastic deformation transition can be identified during the loading process by the pop-in event with a critical load, $P_{\rm crit}$, which is well modeled by all the approaches and can be correlated to experimental results to study stress distributions under the tip. As shown in Fig. 1, the elastic part of the loading process is sensitive to the surface morphology and sample temperature. Results at 300 K show considerable fluctuations around the pop-in point, while these fluctuations disappear when the temperature decreases to 77 K, resulting in more stable data.

In Fig. 2, we report results for the average load of [001] W as a function of the indenter displacement by using different interatomic potentials.

As the indenter tip makes contact with the surface, the force on the indenter increases until the material begins to deform plastically. All approaches report a similar value for the indentation displacement point at 0.9 ± 0.1 showing the elastic to plastic transition, while the critical pop-in load is maximum for EAM and minimum for MEAM, noting the importance of surface information in the approach due to contact responses of the W matrix, regardless of the surface temperature. The effective Young's modulus at 300 K is 420 GPa for EAM and EAM/ZBL, 400 GPa for ABOP and tabGAP, and 355 GPa for MEAM, which is in the experimental range of 350–405 GPa [41]. At 77 K temperature, all the MD simulations resulted in an elastic modulus of 395 ± 5 GPa. This can be attributed to the interaction between the nonatomic RI sphere of the indenter tip, which has a hard sphere, and the W atoms in the top layers of the material, which exhibit only small thermal vibrations. As a result, the elastic behavior modeled by all the methods is similar.

Temperature effects are observed during the elastic part where the interatomic potentials are required to have surface information like surface energy due to the open boundary and plastic deformation initiation by the penetration of the indenter tip in the material. The effect of the crystal orientation is presented in the Supplemental Material (SM) [43], where a sequence is found by every approach used following the characteristic maximum pop-in load for [001] orientation and the minimum one for [111] orientation for BCC metals [2,21,44].

Figure 3 reports the mean contact pressure p, of [001] W to Young's modulus $E_{\rm klm}$, ratio calculated as a linear elastic

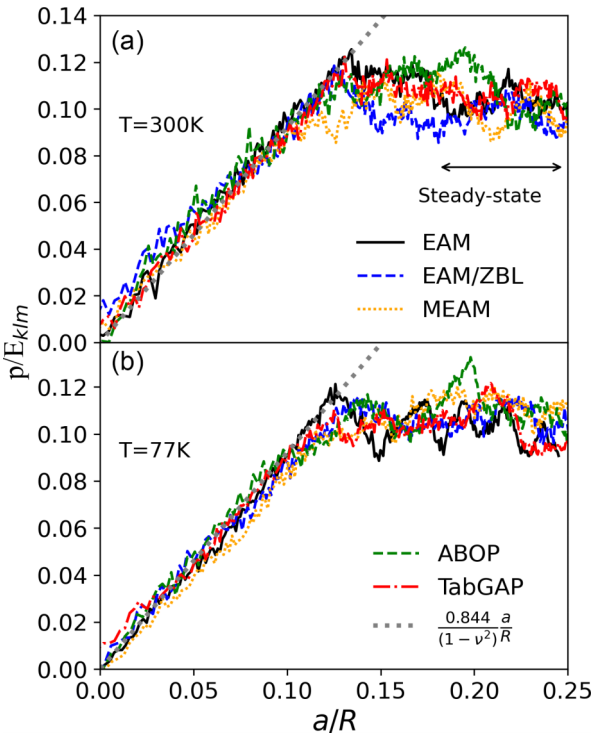

FIG. 3. Evolution of average contact pressure, p, normalized to Young's modulus with normalized contact radius for (011) W by using different approaches at 300 K in (a) and 77 K in (b). Results follow the universal linear relationship as [20] $0.844/(1-\nu^2)a/R_i$, regardless of the employed interatomic potential.

contact mechanics formulation [5,20]:

$$\frac{p}{E_{\rm klm}} = \frac{2\pi}{3E_{\rm klm}}\left[24P\left(\frac{E_{\rm klm}R}{1-\nu^2}\right)^2\right]^{1/3} \tag{6}$$

as a function of the normalized contact radius, a/R, between the sample and the tip with the geometrical relationship $a(h) = [3PR(1-\nu^2)/8E_{\rm klm}]^{1/3}$, which is related to the inner radius of the plastic region where the defects nucleate. The results seem to follow the universal linear relationship as [20] $0.844/(1-\nu^2)a/R_i$, with R_i as the indenter radius for all the approaches with tabGAP results reaching the best agreement, which indicates that the atomic ensembles fulfill coarse-grained, linear elastic contact mechanics and boundary conditions do not affect the simulation dynamics. As observed in Fig. 3, the recorded load curves can be affected by both the spatial arrangement of the surface atoms and the thermally induced atomic vibrations [2]. Thus temperature effects are observed in the elastic part by fluctuations of the mean contact as a response of the interaction of the indenter tip with the W atom at the top layer of the surface sample. Due to the size of the indenter tip, the transitional regime is defined between 0.12 and 0.15 a/R, while the steady state of the loading process is reached at bigger values at both temperatures. The value $p/E_{001} = 0.09 \pm 0.012$ at the steady state is similar to the one reported for (001) Ta and other BCC metals by Varilla *et al.* [20], showing a good agreement between the approaches for calculations of material's hardness.

It is well established that plastic deformation in a material does not initiate at the surface, but rather at some atomic layers' depth below it. This depth is known as the yield point or yield depth at which the material begins to nucleate defects and further dislocations under the applied load or stress [5], within the closest plastic region along the vertical z axis underneath the spherical indenter tip expressed as

$$\sigma_{zz} = -\left(\frac{3F}{2\pi\,\mathrm{a}(h)^2}\right)\left[\left(1-\left|\frac{z}{\mathrm{a}(h)}\right|\arctan\left|\frac{\mathrm{a}(h)}{z}\right|\right)(1+\nu) - \frac{1}{2[1+z^2/\mathrm{a}(h)^2]}\right] \tag{7}$$

as an attempt to determine the strength and stability of the W matrix under load. The stress applied in the direction parallel to the indenter surface is then expressed as

$$\sigma_{xx} = \sigma_{yy} = -\left(\frac{3F}{2\pi\,\mathrm{a}(h)^2}\right)\frac{1}{1+z^2/\mathrm{a}(h)^2}, \tag{8}$$

where x, y, and z are the coordinates in the Cartesian system, ν is the Poisson's ratio, and F is the nanoindentation load. This defines the maximum shear stress as $\tau_{\rm Max} = (\sigma_{zz} - \sigma_{xx})/2$ that the material can withstand before it begins to undergo plastic deformation as reported in Fig. 4, being normalized by the applied pressure (equal to the force F divided by the contact area). The normalized depth is the distance from the surface of the material to the point at which the

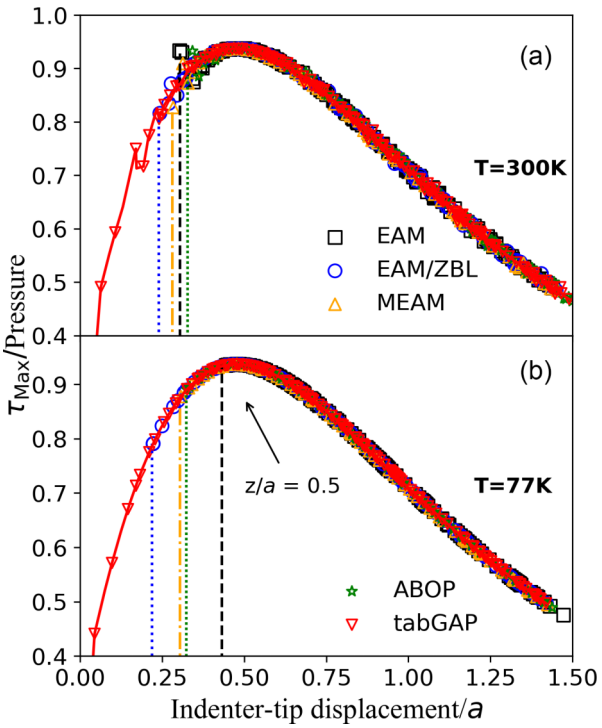

FIG. 4. Hertzian calculation of normalized maximum shear stress by the applied pressure, $\tau_{\rm Max}/P$, as a function of normalized depth at a temperature of 300 K in (a) and 77 K in (b). Surface information is needed in the interatomic potentials to model nanoindentation as observed in the range of 0.2 to 0.49 z/a. The vertical lines indicate the points where $\tau_{\rm Max}$ is not zero, which provides valuable surface information as demonstrated by the tabGAP simulations.

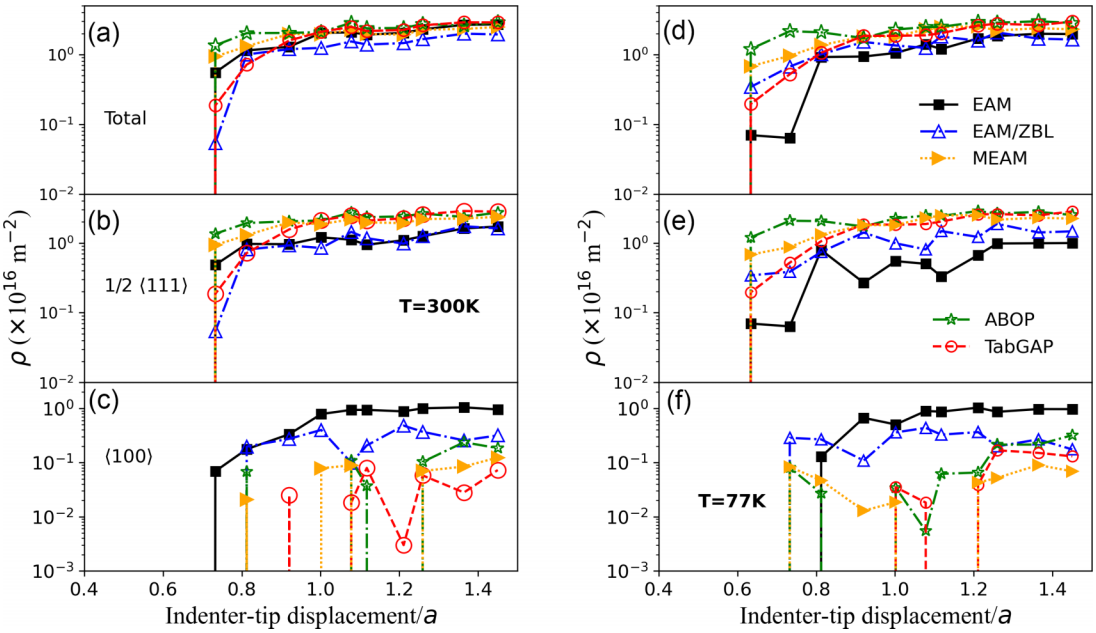

FIG. 5. Average total, $1/2\langle 111\rangle$, and $\langle 100\rangle$ type dislocation density as a function of the normalized indentation depth during loading process at a temperature of 300 K in (a)–(c) and 77 K in (d)–(f), showing the differences of the description of W-W interaction by the MD potentials.

maximum shear stress occurs, normalized by the radius of the indenter that is used to apply the shear forces. Our MD results showed that the point at which plastic deformation begins is at a normalized depth of $z/a = 0.5$ for both temperatures considered. We also observed that the choice of interatomic potential can have an impact on the modeling of the contact between the indenter tip and the surface of the material. Specifically, our findings indicate that the tabGAP method offers a more precise depiction of the interaction between the indenter tip and the surface, exhibiting a smooth increase of the shear stress within the range of 0–0.2 z/a. In contrast, other methods are not able to capture this information.

A. Dislocation nucleation

In general, dislocation glide occurs in the closest-packed $\langle 111\rangle$ directions for BCC metals with Burgers vector $b = 1/2\langle 111\rangle$ and slip planes belong to the $\{110\}$ and $\{112\}$. To analyze the atomic structure during the nanoindentation test which provides information about the mechanisms of dislocation nucleation and evolution [45], we use OVITO [46] with the DXA package [47] to identify dislocations into several dislocation types according to their Burgers vectors as $1/2\langle 111\rangle$, $\langle 100\rangle$, and $\langle 110\rangle$ dislocation types with their corresponding dislocation density, ρ, defined as

$$\rho = \frac{l_{\mathrm{klm}}}{V_D}, \tag{9}$$

where l_{klm} is the dislocation length of each type, by using a hemispherical radius of the plastic zone of $r_{\mathrm{pz}} = a_{\mathrm{pz}}[r^2 - (r-h)^2]^{1/2}$ with $a_{\mathrm{pz}} = 1.9$ and the total volume equal to the hemispherical volume excluding the volume displaced by the indenter tip as $V_D = (2\pi r_{\mathrm{pz}}^3/3) - [\pi h^2(r-h)/3]$, with r as the indenter radius and h the indentation depth, excluding pileup or sink in effects in this model [48].

Figure 5 shows dislocation densities as a function of normalized indentation depth for 300 and 77 K of (001) W samples. Oscillations are observed in the loading process for the densities of both $\langle 111\rangle$ and total dislocations at both temperatures, with minima occurring at 0.9 and 1.1 z/a points, where prismatic loops were observed to nucleate. It is worth noting that the different potentials we used yielded different results for the nucleation and evolution of dislocation junctions at the $\langle 100\rangle$ plane, where a good representation of dislocation glide is important. This mechanism is poorly represented by the EAM and EAM/ZBL methods. We also observed that the formation of this type of defect is common under the indenter tip, where the interaction or dissociation of $1/2\langle 111\rangle$ dislocations can lead to the nucleation of dislocation junctions as $1/2\langle 111\rangle + 1/2\langle \bar{1}\bar{1}1\rangle = \langle 001\rangle$ and other symmetrically geometrical combinations. We observed temperature effects at the point where dislocations begin to nucleate; this difference is likely due to the increased thermal motion of the atoms in the top layer at the higher temperature, which affects the dislocations' mechanisms to nucleate and propagate through the material. In the SM, we report results for the (011) and (111) W matrices with results for those of (001) W.

We visualize the dislocation network nucleated at a depth of $z = 0.9a$ in Fig. 6, where initial half loops are noted, and $z = 1.22a$ in Fig, 7, where prismatic loops evolve through the sample at 77 and 300 K sample temperature. For BCC materials with a (001) orientation, it is well known that the nucleation of prismatic loops is initiated by the formation of shear loops after the yield point [5,20], which then propagate along the expected $\langle 111\rangle$ slip directions. This mechanism was observed in our MD simulations using MEAM, ABOP, and particularly tabGAP [Figs. 6(c) and 6(d)]. Temperature effects on this mechanism are associated with the faster propagation of shear loops at lower temperatures; this is due to the more

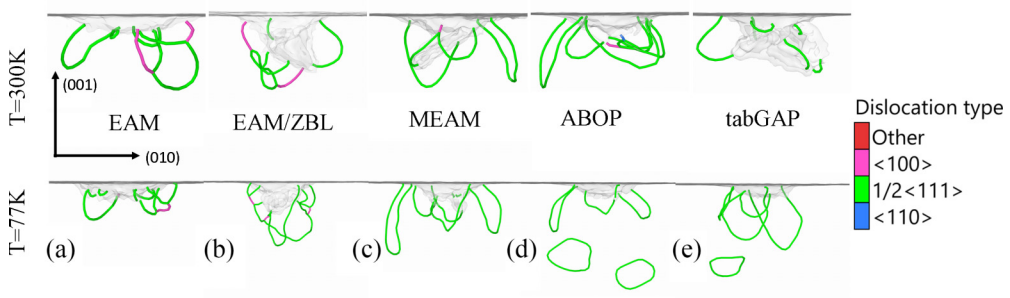

FIG. 6. Visualization of the dislocation nucleation and evolution at depth $z = 0.9a$.

stable lattice positions of the W atoms during the loading process, which leads to the more efficient nucleation of prismatic loops [see Figs. 7(c) and 7(d)]. As the indenter tip goes deeper into the sample, the shear loops expand through the advancement of edge dislocations, while the screw dislocations can undergo limited cross slip, as seen in the simulations using MEAM, ABOP, and tabGAP. This cross slip of the screw dislocations eventually leads to a pinch-off action, resulting in the formation of prismatic loops. It is worth noting that the edge dislocations cannot undergo cross slip. As plastic deformation proceeds during the loading process, the formed prismatic loop advances and the process of shear loop formation and cross slip repeats itself underneath the indenter tip. We noticed that, among the different potentials we used, tabGAP simulations provided the most accurate modeling of this mechanism, showing good qualitative agreement with the results that are expected to be observed in experiments [16,17].

It is well known that dislocation glide in BCC metals is mainly governed by the Peierls barrier, which measures the stress that needs to be applied in order to move a dislocation core to the next atomic valley in the glide plane. Moreover, the Peierls barrier is smaller for edge dislocations than for screw dislocations, where the BCC metal plasticity is dominated by the sluggish glide of screw dislocation segments, as shown by our MD simulations [49,50]. Thus the "lasso" mechanism is observed by all methods for (111) W, suggesting that the main dislocation nucleation mechanism remains analogous to other BCC metals [20,21], with a difference on the number loops nucleated by each approach. In Table III we present the number of prismatic loops nucleated at the maximum indentation depth, quantified for all the potentials we tested at different temperatures. We noticed that ABOP and tabGAP are capable to model the nucleation of dislocation loops on the expected ⟨111⟩ and ⟨112⟩ slip directions. The visualization of the dislocation dynamics during the nanoindentation test for both the (011) and (111) orientations can be found in the Supplemental Material [43].

B. Nanoindentation-induced plastic patterning

The formation of slip traces at the surface is an important aspect of the crystal plasticity process that occurs during a nanoindentation test, as these traces provide evidence of the underlying dislocation glide processes occurring in the subsurface. As shown in Fig. 8, the four ⟨111⟩ slip directions that occur at 300 K temperature lead to the formation of surface pileups with fourfold symmetry. This figure provides a visualization of this process at the maximum indentation depth by using different approaches. The figure includes a color palette that indicates the magnitude of the displacement, revealing that the pileups form around the indenter mark in the shape of a fourfolded rosette due to the (001) orientation of the W matrix, as expected for BCC metals on a (001) orientation. This has been reported experimentally for tungsten by Argus images reported by Yu *et al.* [51], where the surface morphology shows fourfold slip traces on the $(1\bar{1}0)$ and (110) planes. Moreover, large-scale MD simulations for α-Fe [2] have also demonstrated similar pileups resulting from the slip directions.

In Fig. 9, we present the results of von Mises strain atomic mapping at the maximum indentation depth, as obtained from OVITO and reported in our previous work [21]. The sample

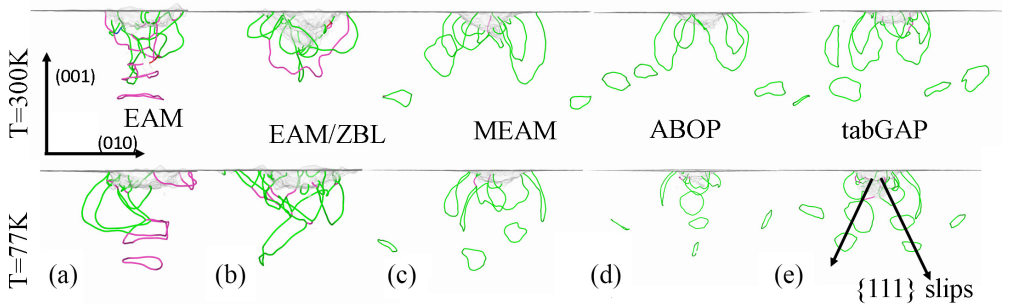

FIG. 7. Visualization of the dislocation nucleation and evolution at depth $z = 1.22a$, using all approaches. Shear dislocation loops are nucleated at the maximum indentation depth in the case of all potentials.

TABLE III. Average number of dislocation loops nucleated at the maximum indentation depth for W by different potentials. Results for temperatures of 300 K and 77 K.

	(001)		(011)		(111)	
Potentials	300 K	77 K	300 K	77 K	300 K	77 K
EAM	1	2	3	4	1	2
EAM/ZBL			2	3	1	2
MEAM	3	4	6	9	4	5
ABOP	4	6	5	6	6	7
tabGAP	4	6	5	7	6	8

was slid on the (011) plane, revealing that the maximum strain follows the ⟨111⟩ slip directions, due to the BCC crystal geometry of the W samples. This highlights the importance of accurate modeling for simulations involving open boundaries. From our MD simulations, the formation of indentation plastic imprints is a process associated to the onset of plastic bursts during mechanical loading that is modeled in a similar manner by tabGAP, ABOP, and the modified EAM potential, where our results are in good agreement with experimental electron microscopy images [17,19,51]. Results for both (011) and (111) orientations can be found in the Supplemental Material [43]. In addition, the dynamics of twin nucleation and twin annihilation during the loading process is a key aspect of the plastic deformation of the W material that needs to be observed in the experimental nanoindentation test. Twin nucleation refers to the process by which a twinned region forms within the W lattice, while twin annihilation refers to the process by which twinned regions transform into dislocations or a dislocation network beneath the indenter tip, as reported experimentally by Wang *et al.* [52] in compression experiments. These processes are generally influenced by the surface energy of the sample, which is a measure of the energy required to create or modify the surface of the material by external load. In our simulations, we utilized the BDA method [53] to identify material defects as twin planes {112} as described in the Appendix A. Although some W atoms were identified as twins in all the simulations, consistent with the literature [44], they can be likely misidentified as screw dislocations. Only in the tabGAP simulations were several W atoms observed in the near vicinity of the indenter tip, which exhibited twin-like defects upon structural analysis and visual examination [see Fig. 8(f)].

There are several machine-learning-based interatomic potentials for W reported in the literature, such as GAP [54] and spectral neighbor analysis potential (SNAP) [55]. However, nanoindentation simulations require simulation cells with

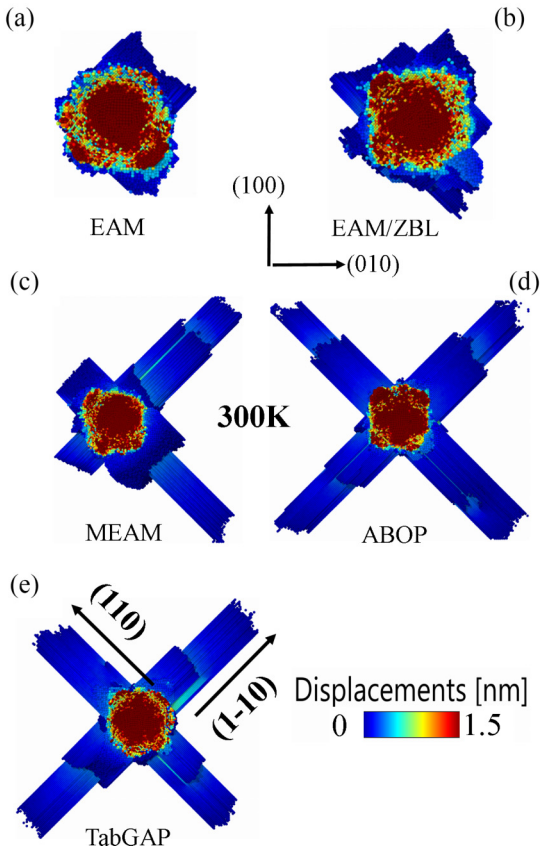

FIG. 8. Visualization of the formation of pileups and slip traces for the indented [001] W sample at the maximum depth (3 nm). The surface morphology for ABOP and tabGAP show fourfold slip traces on the $(1\bar{1}0)$ and (110) planes in good agreement with experimental findings [51].

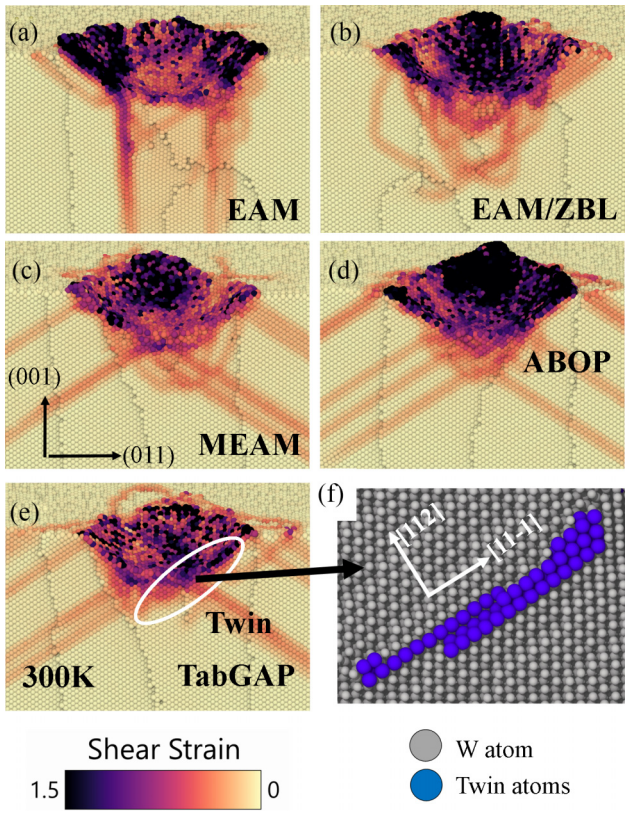

FIG. 9. Visualization of the von Mises strain mapping for the indented [001] W sample at the maximum depth, at room temperature. The W matrix is slid on the (011) plane for better visualization. BCC {112} twin boundaries are identified in our simulations as depicted in (f) by BDA method and are marked by white circles for the tabGAP simulations.

millions of atoms and open boundaries. A single MD simulation using GAP and SNAP potentials would require a wall time of 10–20 days with high computational resource demands, as we tested for our simulation cells. In our work, we are focused on modeling nanoindentation with interatomic potentials that offer the possibility of a good description of the plastic deformation of W matrices with modest computer resources and wall times on the scale of hours. Therefore, we used a Linux cluster with 120 Intel(R) Xeon(R) CPU E5-2680 v2 processors at 2.80 GHz, with wall time of 82 min for the EAM potential, 63 min for the EAM/ZBL potential, 780 min for the MEAM potential, 960 min for the ABOP potential, and 1658 min for the tabGAP potential that seems to model several defect nucleation and evolution mechanisms.

C. Nanoindentation load rate

We have shown that tabGAP simulations provide a reliable description of the mechanism of plastic deformation of W during the loading process. Thus we decided to decrease the load rate to 10 m/s and 5 m/s to give W samples more time to dissipate the energy and yield more ductile behavior. This will give us the opportunity to better understand the nanocontact between the indenter tip and the surface and, consequently, the initiation of plastic deformation, which is of importance in experiments [56]. In Fig. 10, we present the results of the evolution of the average contact pressure, p, normalized to the Young's modulus, at different load rates. Sample temperature is 300 K in (a) and 77 K in (b). It is observed that when indentation goes beyond linear elasticity, the W matrix responds with sudden, first pop-in events characterized by different magnitudes of the load drop, Δp. The load drops mark the early inception of defects and are more pronounced as the load rate decreases, regardless of the sample temperature. We argue that the ratio of the contact pressure, p_c, defined as the point where the drop is identified, to the Young's modulus, E_{klm}, can be used as an intrinsic measure of the surface resistance to dislocation nucleation mechanisms.

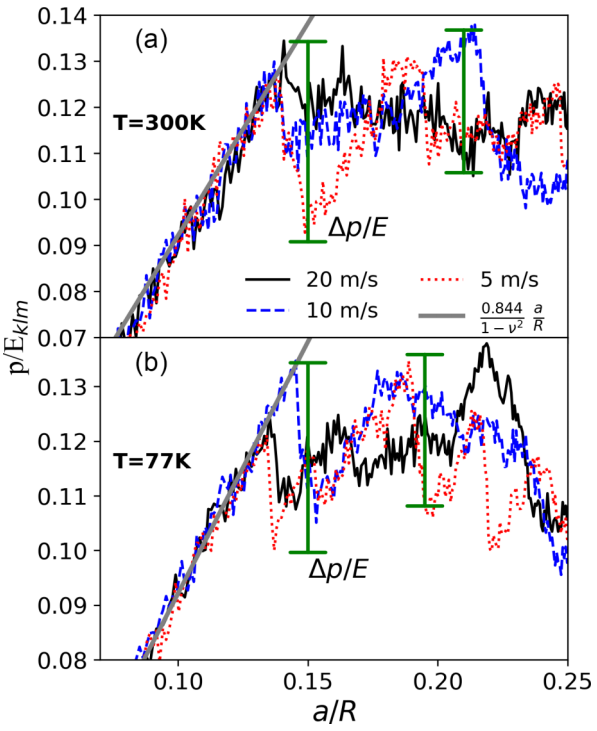

FIG. 10. Evolution of p/E with normalized contact radius at room temperature (a) and 77 K (b) showing the effect of load rate on the nanomechanical response of (001) W. The critical normalized pressure is identified as a deviation from the Hertz fitting and is marked in the figures. This deviation triggers early defect nucleation and is accompanied by the first hardness drop, $\Delta p/E$, and a subsequent second one.

Furthermore, the contact pressure results obtained from our study can be compared qualitatively with the compression experimental stress-strain curves reported by Wang *et al.* [52] (see Fig. 3 in the main text and Fig. S3 in the Supplemental Material for a qualitative comparison to our results). Wang *et al.* demonstrated the antitwinning phenomenon in BCC W nanowires with diameters less than approximately 20 nm during compression, where a transition from dislocation slip to antitwinning shear was observed with decreasing nanowire diameter. This transition was attributed to the limited plastic deformation carriers in nanosized BCC crystals. Our nanoindentation simulations conducted with tabGAP revealed that, at a load rate of 20 m/s and particularly at 5 m/s, a load drop of $\Delta p/E = 0.035$ in a range of 0.13 to 0.15 a/R resulted in ultrahigh stresses that triggered the formation and growth of twins, as shown in Fig. 9.

D. Stacking fault and dislocation glide energies

Generalized stacking fault energy (GSFE) is a measure of the energy required to create a specific defect or deformation in the W lattice, such as a twin or stacking fault. To understand the mechanisms of twin nucleation during loading process, we compute the GSFE for W using different interatomic potentials. The GSFE is computed by cutting a perfect crystal along a specific direction, known as the γ line, and calculating the energy required to move one part of the cut crystal relative to the other. The γ line is parallel to the cut plane and the movement of the two parts of the cut crystal results in the creation of a specific defect or deformation. In our computations, we applied periodic boundary conditions along the cut plane with unit cells from dislocation objects with 2×2 lattice units (l.u.) surface area and 30 l.u. perpendicular to the cut plane. For relaxation, we used a force tolerance of 0.01 eV/Å. Figure 11 shows the results for the GSFE for each displacement vector, where the atomic positions are relaxed only in the direction perpendicular to the cut plane [57]. These results confirmed the different shapes of the slip traces showing that EAM/ZBL potentials subestimate the SFEs, which may explain why this method does not predict the formation of twinned regions. However, MEAM and tabGAP agree well with reported DFT calculations [39] for $\langle 111 \rangle \{110\}$ with a value of $\sim$0.1 eV/Å^2 at the stable point.

In order to evaluate the ability of the applied potentials to model the nucleation and motion of dislocations during loading, we compute the screw and junction dislocation glide energies. These energies measure the resistance of the material to plastic deformation in a specific direction and

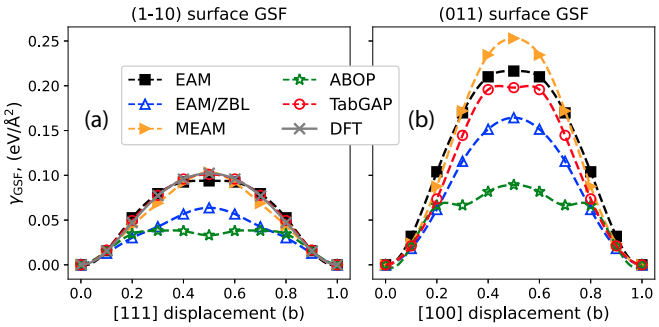

FIG. 11. Generalized stacking fault energies for ⟨111⟩{110} in (a) and ⟨100⟩{011} in (b) computed for all approaches. Data for ⟨111⟩{110} is compared with DFT results from [24].

are calculated by considering the motion of dislocations between two easy cores using the nudged elastic band (NEB) method. A force tolerance of 0.025 eV/Å is used during the minimization process and the initial path of the dislocation is determined using linear interpolation of the atomic positions between the initial and final relaxed configurations with force tolerance of 0.001 eV/Å, which are obtained using anisotropic elasticity within the Stroh formalism [58] using the elastic constants reported in Table I. As presented in Fig. 12, the tabGAP seems to have the overall best compromise with comparable barriers for two-junction dislocation glide planes and reasonable screw dislocation barriers as compared to recent QM/ML results [59]. The other potentials have some inaccuracies: (i) MEAM and EAM/ZBL potentials poorly represent screw dislocation core stability; (ii) EAM and MEAM significantly overestimate the glide barrier for a junction dislocation in the {001} glide plane; (iii) MEAM, ABOP, and EAM/ZBL predict almost zero glide for the junction dislocation in the {011} glide plane. The results obtained can guide experiments in understanding the fundamental mechanisms for nanoindentation induced dislocation nucleation through *in situ* transmission electron microscopy (TEM) images [60].

IV. CONCLUDING REMARKS

This work investigates the nanomechanical response of crystalline W during nanoindentation tests by performing MD simulations with different interatomic potentials: traditional EAM, EAM with ZBL corrections, modified EAM (MEAM), analytic bond-order potential (ABOP), and a recently developed tabulated Gaussian approximation potential (tabGAP). The study analyzes the dislocation nucleation and evolution mechanisms for each approach at different temperatures and loading rates. The nanoindentation loading process is characterized by recording load-displacement curves, dislocation densities, and atom displacement mapping. The comparison of the potentials shows similarities in stress-strain curves, but differences are observed while describing the nanocontact mechanisms between the indenter tip and the surface. Dislocation nucleation mechanisms are differently modeled by the approaches, where prismatic loop nucleation is highly affected by the surface, stacking faults, and dislocation glide energies information for each method. It is also worth noting that the computational time and resources required for performing MD simulations can vary significantly depending on the chosen interatomic potential. The tabGAP simulations were found to be slower than EAM-based simulations, but provided a better modeling for mechanical testing.

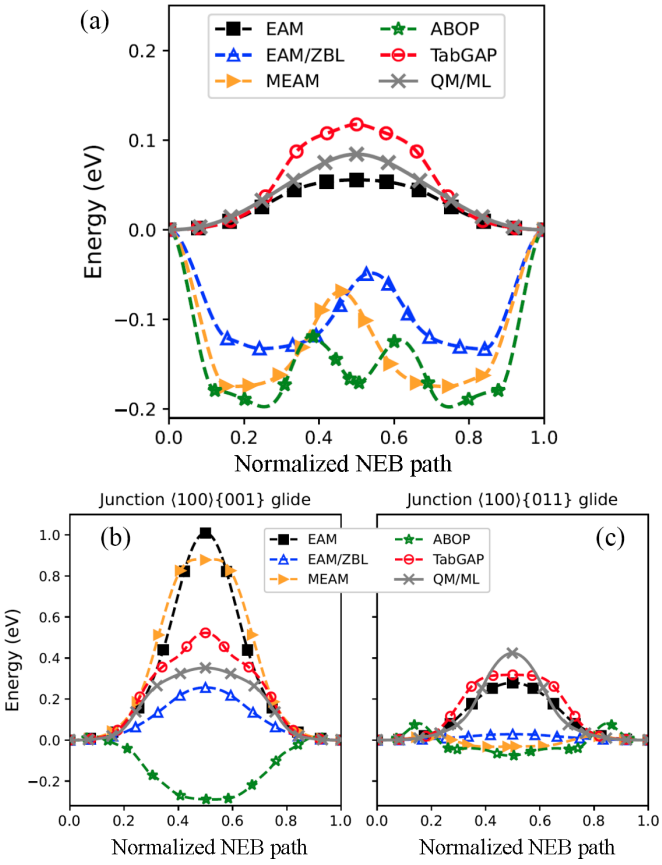

FIG. 12. Screw in (a) and junction in (b) dislocation glide 1/2⟨111⟩{110} energy of crystalline W by NEB method for different MD potentials. We compare to reported results by QM/ML calculations [59].

A general conclusion is that nanomechanical tests can be modeled by several interatomic potentials, with similar load-displacement and stress-strain curves, but dislocation dynamics depends on the approach used being exhibited by NEB calculations of screw and edge dislocation glide of 1/2⟨111⟩{110} and junction ⟨100⟩{001} and ⟨100⟩{110} energies, and stacking fault energies showing that tabGAP simulations can emulate the nanoindentation test as close as possible to experiments. In our future work, we will investigate the nanomechanical response of chemically complex BCC metals under external load by using recently developed tabGAP potentials that can be compared to experimental SEM and TEM images.

ACKNOWLEDGMENTS

We would like to thank M.-C. Marinica and J. Alcalá for inspiring conversations. We acknowledge support from the European Union Horizon 2020 research and innovation program under Grant Agreement No. 857470 and from the European Regional Development Fund via the Foundation for

Polish Science International Research Agenda PLUS program Grant No. MAB PLUS/2018/8. We acknowledge the computational resources provided by the Interdisciplinary Centre for Mathematical and Computational Modelling (ICM) University of Warsaw under computational allocation No. g91–1427. P.G. gratefully recognizes support from the Agence Nationale de Recherche, via the MeMoPAS Project No. ANR-19-CE46-0006-1 as well as access to the HPC resources of IDRIS under the allocations No. A0090910965 and No. A0120913455 attributed by GENCI.

APPENDIX: DEFECTS IDENTIFICATION

In order to identify the defects in nanoindentation simulations, we apply the BCC Defect Analysis (BDA) developed by Möller and Biztek [53], which utilizes coordination number (CN), centrosymmetry parameter (CSP), and common neighbor analysis (CNA) techniques to detect typical defects found in bcc crystals. Then, BDA compares the CN and CSP values of each atom that is not in a BCC perfect lattice point according to CNA or has a CN of 14 with empirically determined values for common defects such as surfaces, vacancies, twin boundaries, screw dislocations, {110} planar faults, and edge dislocations.

The results of the BDA technique used to identify defects in the plastic region beneath the indenter tip of the (001) W sample at 300 K with MD simulation performed by tabGAP are presented in Fig. 13. The developers of BDA have reported that the line direction of screw dislocations corresponds to the shearing direction for producing a deformation twin, making it impossible to differentiate their characteristics from those of twin boundaries. However, since dislocations are line defects, they can easily be distinguished from planar twin structures by comparing their dimensionalities. Although this comparison is not yet implemented in the BDA algorithm, precise defect identification is performed by visual inspection of the analysis output mainly observed beneath the indenter tip. Additionally, CNA can detect twinning dislocations as bcc and characterize them by a relatively high CSP (>8) but less than nine perfect bcc neighbors. Atoms near twin boundaries that lack one neighbor atom have either a low CSP (<1) but four 14-coordinated neighbors with CSP > 8 or a relatively high CSP (>4.5) and a fixed number of perfect, 13-, and 14-coordinated neighbors. This methodology was utilized to identify twin boundaries in our simulation, and it may be the reason why twinning was challenging to model using traditional EAM-based methods.

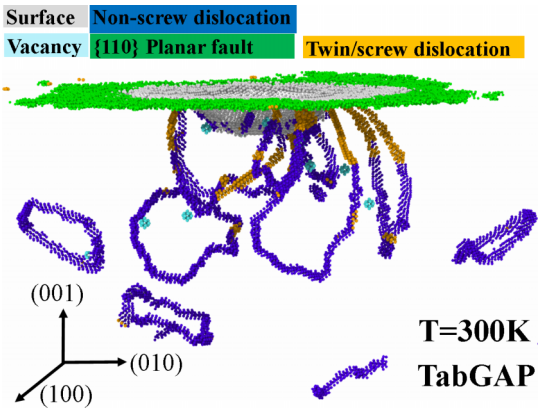

FIG. 13. Defects in the plastic region beneath the indenter tip at the maximum depth of the (001) W sample were identified using the BCC defect analysis (BDA) technique.

[1] C. A. Schuh, Mater. Today **9**, 32 (2006).
[2] J. Varillas, J. Ocenasek, J. Torner, and J. Alcala, Acta Mater. **125**, 431 (2017).
[3] L. Kurpaska, F. J. Dominguez-Gutierrez, Y. Zhang, K. Mulewska, H. Bei, W. J. Weber, A. Kosińska, W. Chrominski, I. Jozwik, R. Alvarez-Donado, S. Papanikolaou, J. Jagielski, and M. Alava, Mater. Des. **217**, 110639 (2022).
[4] S. Pathak and S. R. Kalidindi, Mater. Sci. Eng.: R: Rep. **91**, 1 (2015).
[5] T. Remington, C. Ruestes, E. Bringa, B. Remington, C. Lu, B. Kad, and M. Meyers, Acta Mater. **78**, 378 (2014).
[6] Z. Li, S. Gao, U. Brand, K. Hiller, and H. Wolff, Nanotechnology **31**, 305502 (2020).
[7] M. Mayer, M. Andrzejczuk, R. Dux, E. Fortuna-Zalesna, A. Hakola, S. Koivuranta, K. Krieger, K. J. Kurzydlowski, J. Likonen, and G. Matern, Phys. Scr. **2009**, 014039 (2009).
[8] P. Piaggi, E. Bringa, R. Pasianot, N. Gordillo, M. Panizo-Laiz, J. del RÃo, C. G. de Castro, and R. Gonzalez-Arrabal, J. Nucl. Mater. **458**, 233 (2015).
[9] B. Lipschultz, J. Roth, J. W. Davis, R. P. Doerner, A. A. Haasz, A. Kalenbach, A. Kirschner, R. D. Kolasinski, A. Loarte, V. Philipps, K. Schmid, W. R. Wampler, G. M. Wright and, D. G. Whyte, Tech. Rep. MIT **PSFC/RR**, 10 (2010).
[10] M. Kaufmann and R. Neu, Fusion Eng. Des. **82**, 521 (2007).
[11] T. Schwarz-Selinger, J. Bauer, S. Elgeti, and S. Markelj, Nucl. Mater. Energy **17**, 228 (2018).
[12] R. Pitts, S. Carpentier, F. Escourbiac, T. Hirai, V. Komarov, S. Lisgo, A. Kukushkin, A. Loarte, M. Merola, A. Sashala Naik, R. Mitteau, M. Sugihara, B. Bazylev, and P. Stangeby, J. Nucl. Mater. **438**, S48 (2013), proceedings of the 20th International Conference on Plasma-Surface Interactions in Controlled Fusion Devices.
[13] M. Rieth, J. Boutard, S. Dudarev, T. Ahlgren, S. Antusch, N. Baluc, M.-F. Barthe, C. Becquart, L. Ciupinski, J. Correia, C. Domain, J. Fikar, E. Fortuna, C.-C. Fu, E. Gaganidze, T. Galán, C. García-Rosales, B. Gludovatz, H. Greuner, K. Heinola *et al.*, J. Nucl. Mater. **417**, 463 (2011), proceedings of ICFRM-14.
[14] J. Pamela, A. Bécoulet, D. Borba, J.-L. Boutard, L. Horton, and D. Maisonnier, Fusion Eng. Des. **84**, 194 (2009), proceeding of the 25th Symposium on Fusion Technology.
[15] N. Holtkamp, Fusion Eng. Des. **84**, 98 (2009), proceeding of the 25th Symposium on Fusion Technology.
[16] B. D. Beake and S. Goel, Int. J. Refract. Met. Hard Mater. **75**, 63 (2018).
[17] K. Miyahara, S. Matsuoka, and N. Nagashima, JSME Int. J. Ser. A **41**, 562 (1998).

[18] Z. Wen, G. Xuanqiao, Z. Pingxiang, H. Zhongwu, L. Laiping, and C. Jun, Rare Met. Mater. Eng. **46**, 3626 (2017).

[19] J. Wang, T. Volz, S. Weygand, and R. Schwaiger, J. Mater. Res. **36**, 2166 (2021).

[20] J. Varillas-Delgado and J. Alcala Cabrelles, A molecular dynamics study of nanocontact plasticity and dislocation avalanches in FCC and BCC crystals, Ph.D. dissertation, Universitat Politècnica de Catalunya, Departament de Ciència dels Materials i Enginyeria Metallúrgica, 2019.

[21] F. Domínguez-Gutiérrez, S. Papanikolaou, A. Esfandiarpour, P. Sobkowicza, and M. Alava, Mater. Sci. Eng.: A **826**, 141912 (2021).

[22] G. Po, Y. Cui, D. Rivera, D. Cereceda, T. D. Swinburne, J. Marian, and N. Ghoniem, Acta Mater. **119**, 123 (2016).

[23] E. Tadmor, R. Elliott, J. Sethna, R. E. Miller, and C. A. Becker, JOM **63**, 17 (2011).

[24] M.-C. Marinica, L. Ventelon, M. R. Gilbert, L. Proville, S. L. Dudarev, J. Marian, G. Bencteux, and F. Willaime, J. Phys.: Condens. Matter **25**, 395502 (2013).

[25] U. Bhardwaj, A. E. Sand, and M. Warrier, J. Nucl. Mater. **569**, 153938 (2022).

[26] L.-F. Wang, X. Shu, G.-H. Lu, and F. Gao, J. Phys.: Condens. Matter **29**, 435401 (2017).

[27] D. R. Mason, D. Nguyen-Manh, and C. S. Becquart, J. Phys.: Condens. Matter **29**, 505501 (2017).

[28] G. J. Ackland and R. Thetford, Philos. Mag. A **56**, 15 (1987).

[29] P. Hiremath, S. Melin, E. Bitzek, and P. A. Olsson, Comput. Mater. Sci. **207**, 111283 (2022).

[30] C. Barrett and R. Carino, Integr. Mater. Manuf. Innov. **5**, 177 (2016).

[31] N. Juslin, P. Erhart, P. Träskelin, J. Nord, K. O. E. Henriksson, K. Nordlund, E. Salonen, and K. Albe, J. Appl. Phys. **98**, 123520 (2005).

[32] G. C. Abell, Phys. Rev. B **31**, 6184 (1985).

[33] J. Byggmästar, K. Nordlund, and F. Djurabekova, Phys. Rev. Mater. **6**, 083801 (2022).

[34] A. Glielmo, C. Zeni, and A. De Vita, Phys. Rev. B **97**, 184307 (2018).

[35] J. Vandermause, S. B. Torrisi, S. Batzner, Y. Xie, L. Sun, A. M. Kolpak, and B. Kozinsky, npj Comput. Mater. **6**, 20 (2020).

[36] J. Byggmästar, K. Nordlund, and F. Djurabekova, Phys. Rev. B **104**, 104101 (2021).

[37] F. Dominguez-Gutierrez, Nucl. Instrum. Methods Phys. Res., B **512**, 38 (2022).

[38] A. P. Thompson, H. M. Aktulga, R. Berger, D. S. Bolintineanu, W. M. Brown, P. S. Crozier, P. J. in 't Veld, A. Kohlmeyer, S. G. Moore, T. D. Nguyen, R. Shan, M. J. Stevens, J. Tranchida, C. Trott, and S. J. Plimpton, Comput. Phys. Commun. **271**, 108171 (2022).

[39] X. Wang, S. Xu, W.-R. Jian, X.-G. Li, Y. Su, and I. J. Beyerlein, Comput. Mater. Sci. **192**, 110364 (2021).

[40] R. W. Hertzberg, *Deformation and Fracture Mechanics of Engineering Materials* (Wiley, New York, 1996).

[41] CiDRA Precision Services—Machining of Materials, Tungsten, https://www.azom.com/article.aspx?ArticleID=614.

[42] J. Guénolé, W. G. Nöhring, A. Vaid, F. Houllé, Z. Xie, A. Prakash, and E. Bitzek, Comput. Mater. Sci. **175**, 109584 (2020).

[43] See Supplemental Material at http://link.aps.org/supplemental/10.1103/PhysRevMaterials.7.043603 for (i) lD curves and pile-ups formation of (011) and (111) crystal orientations, (ii) structural analysis of W sample with tab gap, and (iii) principal shear stress calculations.

[44] S. Goel, G. Cross, A. Stukowski, E. Gamsjäger, B. Beake, and A. Agrawal, Comput. Mater. Sci. **152**, 196 (2018).

[45] A. D. Backer, D. Mason, C. Domain, D. Nguyen-Manh, M.-C. Marinica, L. Ventelon, C. Becquart, and S. Dudarev, Nucl. Fusion **58**, 016006 (2018).

[46] A. Stukowski, Modell. Simul. Mater. Sci. Eng. **18**, 015012 (2010).

[47] A. Stukowski, V. V. Bulatov, and A. Arsenlis, Modell. Simul. Mater. Sci. Eng. **20**, 085007 (2012).

[48] C. Begau, J. Hua, and A. Hartmaier, J. Mech. Phys. Solids **60**, 711 (2012).

[49] P. Grigorev, T. D. Swinburne, and J. R. Kermode, Phys. Rev. Mater. **4**, 023601 (2020).

[50] T. D. Swinburne and S. L. Dudarev, Phys. Rev. Mater. **2**, 073608 (2018).

[51] H. Yu, S. Das, H. Yu, P. Karamched, E. Tarleton, and F. Hofmann, Scr. Mater. **189**, 135 (2020).

[52] J. Wang, Z. Zeng, M. Wen, Q. Wang, D. Chen, Y. Zhang, P. Wang, H. Wang, Z. Zhang, S. X. Mao, and T. Zhu, Sci. Adv. **6**, eaay2792 (2020).

[53] J. J. Möller and E. Bitzek, MethodsX **3**, 279 (2016).

[54] W. J. Szlachta, A. P. Bartók, and G. Csányi, Accuracy and transferability of gap models for tungsten, arXiv:1405.4370.

[55] M. A. Wood and A. P. Thompson, Quantum-accurate molecular dynamics potential for tungsten, arXiv:1702.07042.

[56] V. Maier, K. Durst, J. Mueller, B. Backes, H. W. Happel, and M. Gaken, J. Mater. Res. **26**, 1421 (2011).

[57] L. Ventelon and F. Willaime, Philos. Mag. **90**, 1063 (2010).

[58] A. N. Stroh, Philos. Mag. **3**, 625 (1958).

[59] P. Grigorev, A. M. Goryaeva, M. C. Marinica, J. R. Kermode, and T. D. Swinburne, Acta Mater. **247**, 118734 (2023).

[60] B. Wang, Z. Zhang, J. Cui, N. Jiang, J. Lyu, G. Chen, J. Wang, Z. Liu, J. Yu, C. Lin, F. Ye, and D. Guo, ACS Appl. Mater. Interfaces **9**, 29451 (2017).